Adaptive Antenna Pattern Modeling for Interference Mitigation in Radio Astronomy

Ramonika Sengupta, Graduate Student Member, IEEE, and Steven W. Ellingson, Senior Member, IEEE

Abstract—This paper describes methods for accurate pattern modeling of large axisymmetric paraboloidal focus-fed reflector antenna systems. We demonstrate that the incorporation of the developed pattern models helps in advancing the state-of-theart in coherent time-domain canceling (CTC) for interference mitigation in radio astronomy. The first method yields a closedform expression for the antenna pattern with parameters accounting for the focal ratio and feed pattern. In subsequent adaptive methods, parameters of this model are calculated using measurements of interference signals. The corrected pattern model improves the prediction of the change in the true pattern for future times. The methods are compared by (1) comparing the error in the pattern model with respect to the true pattern and (2) comparing the pattern value update period required to achieve a specified level of residual interference when used in CTC. The efficacy of the pattern modeling methods is demonstrated by showing that the error in the pattern model decreases and the pattern value needs to be updated at a much slower rate for effective CTC.

Index Terms—Aperture antennas, Pattern model, Radiation patterns, Receiving antennas, Time domain canceling.

I. Introduction

OHERENT time-domain canceling (CTC) has been proposed to mitigate satellite interference to radio telescopes (see e.g., [1] and references therein). A generic highlevel block diagram of CTC is shown in Fig. 1. In this method, an estimate of the interference signal is generated and is subtracted from the measured signal contaminated with the interference signal. The "estimate interference waveform" block requires a certain time τ to develop an estimate of the interference. A precise knowledge of the antenna pattern is required for the accurate estimation of interference signal because the interference signal is seen through the antenna pattern, which imposes a quickly timevarying channel due to the motion of the satellite [2], [3]. The maximum time duration over which the stationarity of the pattern can be assumed is potentially less than the value of τ assumed in the past work (see e.g., [3] and references therein). This is the limitation of the state-of-the-art in CTC.

The present work addresses the problem of lack of pattern knowledge by developing accurate pattern models and using them in a modified CTC scheme (shown in Fig. 2). We start by developing a new method for obtaining a closed-form pattern model for large focus-fed axisymmetric reflector antenna. This pattern model is then extended using adaptive pattern modeling where we adjust the model based on the

This work was supported in part by National Science Foundation Grants ECCS-2029948 and AST-2128506.



Fig. 1. A high-level generic block diagram of time-domain canceling (CTC).

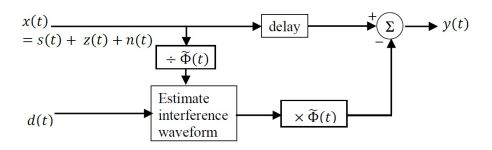


Fig. 2. A high-level generic block diagram of CTC with pattern variation correction.

measurements from the interferer. We have shown that the pattern model can be significantly improved using measurements of the interference signal in real time. In the earlier work [2], the effect of pattern variation on CTC performance is discussed and an analytical expression is derived for the time scale τ required for updating the pattern value. Here we have evaluated the degree to which τ can be increased in CTC by incorporating the developed pattern models in the modified CTC scheme with pattern correction (Fig. 2). The performance of CTC improves with the incorporation of the developed pattern models, and thereby advancing the state-of-the-art in CTC for interference mitigation.

The paper is organized as follows: A new approximate closed-form pattern model for large focus-fed axisymmetric paraboloidal reflector is developed in Section II. This section also gives the comparison of the pattern obtained by this method to the pattern calculated by physical optics (PO) and confirms the validity of the model. To further improve the pattern model, an adaptive method is outlined in Section III with model parameters calculated using measurements of the interference signals. The conclusions are given in Section IV.

II. FAST APPROXIMATE PREDICTION METHOD FOR ANTENNA PATTERN MODELING

We consider an axisymmetric paraboloidal focus-fed reflector antenna having circular physical aperture. For the aperture electric field distributions associated with such systems, the pattern can be expressed approximately in closed form using expressions from [4] (Sec. 9.5.2). For zero edge illumination, the normalized pattern is given as:

$$F(\theta, n) = \frac{2^{n+1}\Gamma(n+2) J_{n+1}(\beta a \sin \theta)}{(\beta a \sin \theta)^{n+1}}$$
(1)

where θ is the angle from the reflector axis of rotation, n determines the specific distribution, J_n is the Bessel function of the first kind and n^{th} order, a is the radius of the aperture, and $\beta(=2\pi/\lambda)$ is wavenumber.

R. Sengupta is with the Department of Electrical Engineering, Eindhoven University of Technology, 5600 MB Eindhoven, The Netherlands. e-mail: r.sengupta@tue.nl.

S. W. Ellingson is with the Bradley Department of Electrical and Computer Engineering, Virginia Tech, Blacksburg, VA, 24061 USA. e-mail: ellingson@vt.edu

For non-zero edge illumination (i.e., normalized aperture field C at the reflector edge), the normalized pattern for parabolic-on-a-pedestal distribution is given as:

$$F(\theta, n, C) = \underbrace{\frac{C}{C + \frac{1 - C}{n + 1}}}_{A_0} F(\theta, n = 0) + \underbrace{\frac{\frac{1 - C}{n + 1}}{C + \frac{1 - C}{n + 1}}}_{B_0} F(\theta, n)$$

$$= A_0 F(\theta, n = 0) + B_0 F(\theta, n) \tag{2}$$

where A_0 and B_0 are real-valued coefficients that are independent of θ . Also, n and C do not change. The on-axis gain $G(=4\pi\varepsilon_{ap}A_p/\lambda^2)$ of the system is determined using the aperture efficiency ε_{ap} and the physical area $A_p (= \pi a^2)$ of the aperture. The aperture efficiency ε_{ap} is determined from the feed pattern and is used to estimate the value of n.

We consider the reflector system with D=18 m, $\nu=1.5$ GHz. For comparison with true pattern $\tilde{\Phi}(\theta)$, we consider the unnormalized model pattern $\sqrt{G}F(\theta)$ for the estimated values of n and C. In general, $|\Phi(\theta)|$ and $|\sqrt{G}F(\theta)|$ are similar (see e.g., Fig. 3), but with significant differences. Thus the potential benefit for the pattern correction is confirmed.

In summary, this method yields a closed-form expression (2) for the antenna pattern with parameters accounting for the focal ratio and feed pattern. However, it may not give a sufficiently close fit for our intended application [2]. To improve this method, an adaptive correction of the pattern function can be done as discussed in the following section.

III. ADAPTIVE PATTERN MODELING

Now we consider whether the true pattern $\Phi(\theta)$ can be accurately modeled using (2) with different coefficients determined from measurements of the true pattern. Hence we define a model pattern $\Phi(\theta)$ as:

$$\Phi(\theta) = A F(\theta, n = 0) + B F(\theta, n)$$
(3)

where A and B are constants that can be determined by comparing $\Phi(\theta)$ to $\Phi(\theta)$. Note that $\Phi(\theta)$ (and subsequently $\Phi(\theta)$) are not normalized; specifically, A and B may represent the gain as well as the shape of the pattern. Since $\Phi(\theta)$ is in general complex-valued, the values of A and B will also be complex.

In the following subsections, we consider the adaptive correction methods in increasing order of complexity.

A. One-point (p = 1) Correction

We use only one measurement, $\tilde{\Phi}(\theta_1)$ at angle θ_1 , and choose A and B such that $\Phi(\theta_1) = \tilde{\Phi}(\theta_1)$. Thus:

$$A F(\theta_1, n = 0) + B F(\theta_1, n) = \tilde{\Phi}(\theta_1)$$
(4)

Pattern modeling using one-point correction is an underdetermined problem with one equation and two unknowns. Hence there are multiple solutions with multiple possible choices of A and B that satisfy the constraint at θ_1 . However, it is not immediately clear which solutions would yield a reasonable fit over the entire pattern. We now examine two solutions that are readily apparent.

In the first solution:

$$A = A_0 \frac{\tilde{\Phi}(\theta_1)}{F(\theta_1, n = 0)};$$

$$B = B_0 \frac{\tilde{\Phi}(\theta_1)}{F(\theta_1, n)}$$
(6)

$$B = B_0 \frac{\tilde{\Phi}(\theta_1)}{F(\theta_1, n)} \tag{6}$$

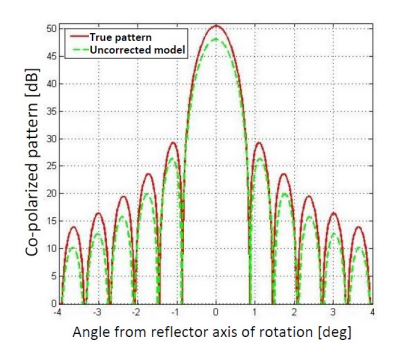


Fig. 3. Comparison of true pattern $|\tilde{\Phi}(\theta)|$ from PO, and uncorrected model pattern $|\sqrt{G}F(\theta)|$.

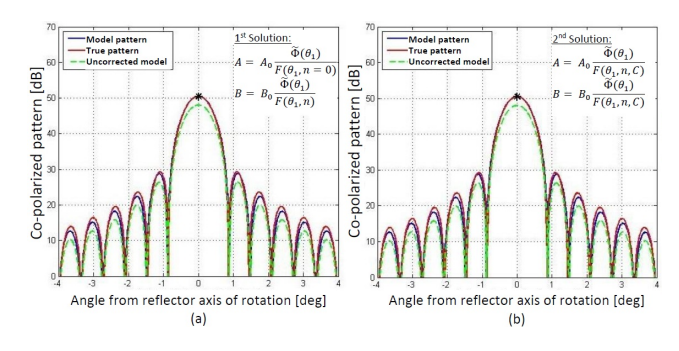


Fig. 4. Comparison of model pattern $|\Phi(\theta)|$ from one-point correction (with θ_1 selected at peak of main lobe marked with "*", true pattern $|\tilde{\Phi}(\theta)|$, and uncorrected model pattern $|\sqrt{GF(\theta)}|$.

In the second solution:

$$A = A_0 \frac{\tilde{\Phi}(\theta_1)}{F(\theta_1, n, C)};$$

$$B = B_0 \frac{\tilde{\Phi}(\theta_1)}{F(\theta_1, n, C)}$$
(8)

$$B = B_0 \frac{\Phi(\theta_1)}{F(\theta_1, n, C)} \tag{8}$$

Fig. 4 shows both solutions with θ_1 selected at the peak of the main lobe. Note that the model patterns $\Phi(\theta)$ obtained from both solutions result in a reasonable fit to the true pattern $\Phi(\theta)$. Fig. 5 shows both solutions applied to θ_1 selected at the peak of the first sidelobe to the right of the main lobe. In this case, the model pattern $\Phi(\theta)$ obtained from the second solution (i.e., (7) and (8)) results in a reasonable fit to $\Phi(\theta)$, whereas the first solution (i.e., (5) and (6)) does

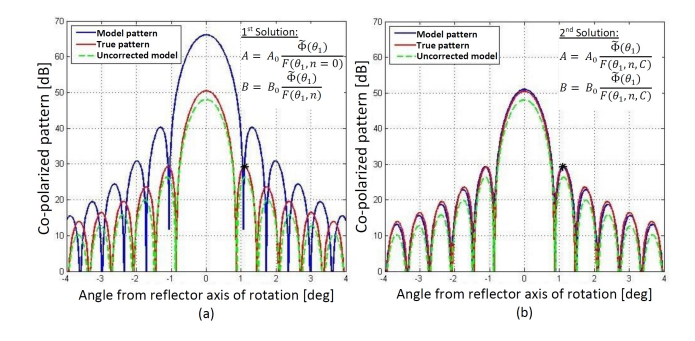


Fig. 5. Comparison of model pattern $|\Phi(\theta)|$ from one-point correction (with θ_1 selected at peak of sidelobe marked with "*", true pattern $|\tilde{\Phi}(\theta)|$, and uncorrected model pattern $|\sqrt{GF(\theta)}|$.

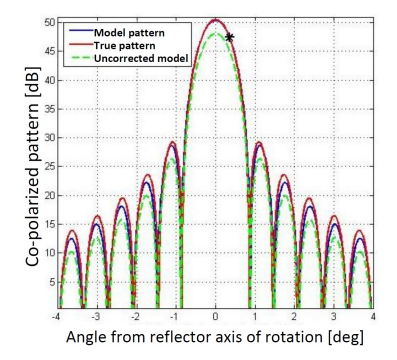


Fig. 6. Model pattern $|\Phi(\theta)|$ from one-point correction (at the -3 dB point at $\theta=+0.35^\circ$, marked with "*"), true pattern $|\tilde{\Phi}(\theta)|$, and uncorrected model pattern $|\sqrt{G}F(\theta)|$.

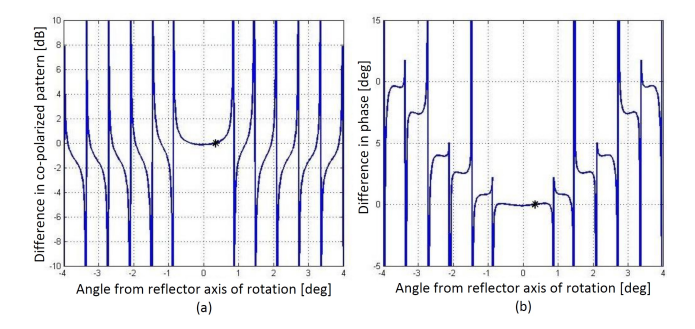


Fig. 7. Difference in (a) magnitude; (b) phase between model pattern $\Phi(\theta)$ obtained from one-point correction (at the -3 dB point at $\theta=+0.35^{\circ}$, marked with "*") and true pattern $\tilde{\Phi}(\theta)$.

Experimentation using other values of θ_1 shows that $\Phi(\theta)$ obtained from the second solution results in a good fit to $\tilde{\Phi}(\theta)$ for θ_1 selected anywhere on the pattern other than null points. On the other hand, $\Phi(\theta)$ obtained from the first solution does not fit well to $\tilde{\Phi}(\theta)$ in many of these cases. A possible reason why the second solution seems to be better might be that the coefficients in the second solution account for the edge illumination C whereas the coefficients in the first solution do not. In rest of the paper, we use the second solution (i.e., (7) and (8)) exclusively for p=1 correction.

Now consider an example of p=1 correction applied at a point on the main lobe between peak and null; e.g., at the -3 dB point at $\theta_1=+0.35^\circ$ as shown in Fig. 6. Fig. 7 shows the difference in magnitude and phase of $\Phi(\theta)$ and $\tilde{\Phi}(\theta)$. The magnitude and phase values of $\Phi(\theta)$ and $\tilde{\Phi}(\theta)$ match exactly at the point where correction is applied, as expected. Fig. 7(a) shows that the error in $\Phi(\theta)$ becomes maximum at the nulls. Fortunately, the error in the nulls is not really of interest in the interference canceling application because the response to satellites is already very small there. Fig. 7(b) shows that the error in the phase of $\Phi(\theta)$ does not vary much within each lobe, but does increase with increasing sidelobe.

A comparison with Fig. 3 shows that p=1 correction method significantly reduces the error in the magnitude of the pattern model $\Phi(\theta)$ (i.e., difference in magnitude of $\Phi(\theta)$ and $\tilde{\Phi}(\theta)$) as compared to the error in the uncorrected pattern model $|\sqrt{G}F(\theta)|$. For constraint angle θ_1 selected at the peaks of main lobe (i.e., $\theta_1=0^\circ$) and first sidelobe (i.e., $\theta_1=1.10^\circ$), the maximum error within the HPBW occurs at the edge of the range (e.g., $\theta=\pm 0.35^\circ$).

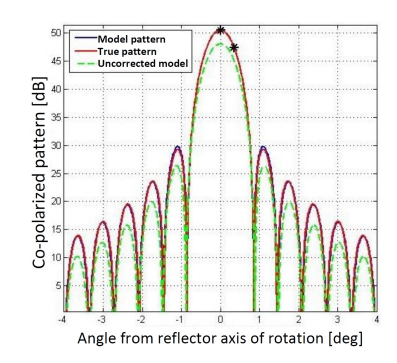


Fig. 8. Model pattern $|\Phi(\theta)|$ from two-point correction (using two points on the main lobe marked with "*"), true pattern $|\tilde{\Phi}(\theta)|$ and uncorrected model pattern $|\sqrt{G}F(\theta)|$.

B. Two-point (p = 2) Correction

While one-point correction clearly improves the agreement between the model pattern and the true pattern, this is true mainly in the angular region around the constrained angle. For better overall fitting, especially at angles far from the measured angle, multiple point correction should be considered. We now consider the two-point correction (p=2) of the pattern.

For p=2, we use two measurements $\tilde{\Phi}(\theta_1)$ and $\tilde{\Phi}(\theta_2)$ at two angles θ_1 and θ_2 . We constrain $\Phi(\theta_1)=\tilde{\Phi}(\theta_1)$ and $\Phi(\theta_2)=\tilde{\Phi}(\theta_2)$ by solving the following linear system of equations:

$$\tilde{\Phi}(\theta_1) = A F(\theta_1, n = 0) + B F(\theta_1, n) \tag{9}$$

$$\tilde{\Phi}(\theta_2) = A F(\theta_2, n = 0) + B F(\theta_2, n) \tag{10}$$

In this case, we have a single solution:

$$A = \frac{\tilde{\Phi}(\theta_1) F(\theta_2, n) - \tilde{\Phi}(\theta_2) F(\theta_1, n)}{F(\theta_1, n = 0) F(\theta_2, n) - F(\theta_2, n = 0) F(\theta_1, n)}$$
(11)

$$B = -\frac{\tilde{\Phi}(\theta_1) F(\theta_2, n = 0) - \tilde{\Phi}(\theta_2) F(\theta_1, n = 0)}{F(\theta_1, n = 0) F(\theta_2, n) - F(\theta_2, n = 0) F(\theta_1, n)}$$
(12)

The two-point correction method reduces the error in pattern modeling as compared to the one-point correction method. This can be seen by considering the following two examples.

Fig. 8 shows an example of two-point correction applied for θ_1 and θ_2 both on the main lobe. These points are the same as those used for one-point correction in Figs. 4(b) and 6; i.e., $\theta_1=0.00^\circ$ and $\theta_2=+0.35^\circ$ respectively. The maximum error in pattern magnitude decreases from 1.96 dB in the first sidelobe (specifically 1.85 dB at $\theta_1=0.00^\circ$ and 1.96 dB at $\theta_1=0.35^\circ$) with one-point correction to 0.78 dB with two-point correction.

Two-point correction applied to the angles $\theta_1 = 0.00^\circ$ and $\theta_2 = +1.10^\circ$, corresponding to the peaks of main lobe and first sidelobe, is shown in Fig. 9. These angles were considered for one-point correction in Figs. 4(b) and 5(b). The maximum error in pattern magnitude decreases from 0.66 dB with one-point correction to 0.06 dB with two-point correction within the HPBW of the main lobe. The maximum error also decreases from 1.85 dB to 0.62 dB within -3 dB region of the first sidelobe.

In conclusion, it is observed that the two-point correction method further reduces the error in the magnitude and phase

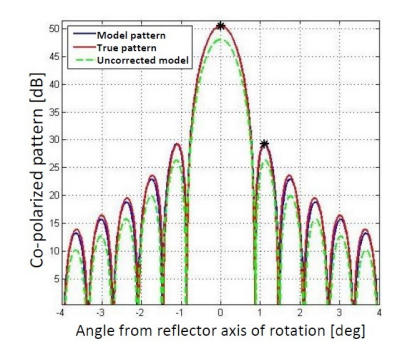


Fig. 9. Model pattern $|\Phi(\theta)|$ from two-point correction (using two points on the peaks of main lobe first sidelobe marked with "*"), true pattern $|\tilde{\Phi}(\theta)|$ and uncorrected model pattern $|\sqrt{G}F(\theta)|$.

within main lobe and sidelobes as compared to the one-point correction method.

C. Multi-point (p > 2) Correction

Now we consider the extent to which additional measurements may yield further improvement in the agreement between the model pattern and the true pattern. The correction methods can be extended for the values of $\tilde{\Phi}(\theta)$ at more than 2 angles; i.e., given measurements $\tilde{\Phi}(\theta_1), \tilde{\Phi}(\theta_2), \cdots, \tilde{\Phi}(\theta_p)$, at $\theta_1, \theta_2, \cdots, \theta_p$. The linear system of equations becomes:

$$\begin{bmatrix}
F(\theta_{1}, n = 0) & F(\theta_{1}, n) \\
F(\theta_{2}, n = 0) & F(\theta_{2}, n) \\
\vdots & \vdots \\
F(\theta_{p}, n = 0) & F(\theta_{p}, n)
\end{bmatrix}
\underbrace{\begin{bmatrix}
A \\
B
\end{bmatrix}}_{\mathbf{x}} = \underbrace{\begin{bmatrix}
\tilde{\Phi}(\theta_{1}) \\
\tilde{\Phi}(\theta_{2}) \\
\vdots \\
\tilde{\Phi}(\theta_{p})
\end{bmatrix}}_{\mathbf{y}}$$

$$\mathbf{M}\mathbf{x} = \mathbf{y} \tag{14}$$

The matrix \mathbf{x} consists of the coefficients we seek and \mathbf{y} consists of the measured pattern values. For p > 2, the system is overdetermined. We can still find a least-squares solution of (14) in the sense that \mathbf{x} minimizes $||\mathbf{y} - \mathbf{M}\mathbf{x}||^2$:

$$\mathbf{x} = (\mathbf{M}^T \mathbf{M})^{-1} \mathbf{M}^T \mathbf{y} \tag{15}$$

Fig. 10 shows how performance changes with increasing number of measurements in a practical scenario, where the number of measurements increase over time. From Sections III-A and III-B, we expect that p=2 correction would yield a better fit than p=1 correction, however, this is not the case when constraint points do not lie in the main lobe. Tables I and II summarize the error of $\Phi(\theta)$ compared to $\tilde{\Phi}(\theta)$ for scenarios in Fig. 10. We observe:

- Although p=2 yields a better fit than p=1 around the far sidelobes (viz., 0.00 dB as opposed to -1.69 dB) where the constraint points are selected. However, p=1 yields a better fit than p=2 in the main lobe (viz., -0.39 dB as opposed to -3.27 dB) and first sidelobes (viz., -2.23 dB as opposed to +2.71 dB).
- Significant improvement is observed for p = 6 and p =
 7; i.e., once constraint points include the first sidelobe and main lobe.
- For p=7 having one constraint point in the main lobe, multi-point correction is better than p=1 correction using the same point in the main lobe.

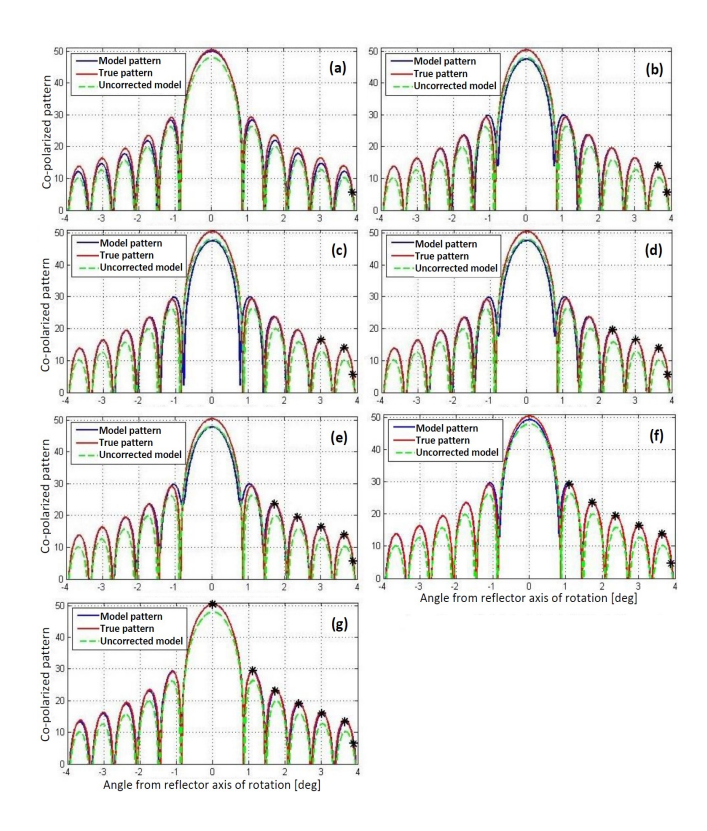


Fig. 10. Model pattern $|\Phi(\theta)|$ obtained from adaptive correction (using points $\theta_1=+3.89^\circ, \theta_2=+3.64^\circ, \ \theta_3=+3.01^\circ, \ \theta_4=+2.37^\circ, \ \theta_5=+1.73^\circ, \ \theta_6=+1.10^\circ, \ \theta_7=0.00^\circ$ marked with "*"), true pattern $|\tilde{\Phi}(\theta)|$ and uncorrected model pattern $|\sqrt{G}F(\theta)|$.

Therefore increasing p can significantly improve performance, even if the additional points are in the sidelobes.

TABLE I Error in $|\Phi(\theta)|$ compared to $|\tilde{\Phi}(\theta)|$ at peaks for points considered in Fig. 10.

	Maximum error at the peaks of					
Scenario	main lobe	right sidelobes				
		first	second	third	fourth	fifth
p = 1	-0.39 dB	-0.87 dB	-1.63 dB	-1.72 dB	-1.71 dB	-1.69 dB
p = 2	-2.88 dB	+0.70 dB	+0.12 dB	+0.03 dB	0.00 dB	0.00 dB
p = 3	-2.90 dB	+0.70 dB	+0.12 dB	+0.03 dB	+0.01 dB	0.00 dB
p = 4	-2.81 dB	+0.69 dB	+0.11 dB	+0.02 dB	−0.00 dB	+0.01 dB
p = 5	-2.57 dB	+0.65 dB	+0.07 dB	−0.02 dB	-0.04 dB	-0.04 dB
p = 6	-1.06 dB	+0.21 dB	+0.35 dB	−0.40 dB	−0.39 dB	−0.38 dB
p = 7	0.00 dB	+0.15 dB	-0.50 dB	−0.57 dB	−0.56 dB	-0.54 dB

TABLE II ERROR IN $|\Phi(\theta)|$ COMPARED TO $|\tilde{\Phi}(\theta)|$ FOR POINTS CONSIDERED IN FIG. 10.

	Error at	Maximum error and its location			
Scenario	$\theta = 0^{\circ}$	in main lobe	within -3d	ithin -3dB points in	
		within HPBW	first left sidelobe	first right sidelobe	
p = 1	-0.39 dB	−0.39 dB, 0.00°	-2.23 dB, -0.97°	−2.23 dB, +0.97°	
p = 2	-2.88 dB	-3.27 dB, +0.35°	$+2.71 \text{ dB}, -0.97^{\circ}$	$+2.71 \text{ dB}, +0.97^{\circ}$	
p = 3	-2.90 dB	−3.30 dB, +0.35°	$+2.70 \text{ dB}, -0.97^{\circ}$	$+2.70 \text{ dB}, +0.97^{\circ}$	
p = 4	-2.81 dB	$-3.19 \text{ dB}, +0.35^{\circ}$	$+2.70 \text{ dB}, -0.97^{\circ}$	$+2.70 \text{ dB}, +0.97^{\circ}$	
p = 5	-2.57 dB	$-2.87 \text{ dB}, +0.35^{\circ}$	$+2.68 \text{ dB}, -0.97^{\circ}$	$+2.68 \text{ dB}, +0.97^{\circ}$	
p = 6	-1.06 dB	−1.15 dB, +0.35°	+0.98 dB, −0.97°	+0.98 dB, +0.97°	
p = 7	0.00 dB	+0.04 dB, +0.35°	$+0.66 \text{ dB}, -1.26^{\circ}$	$+0.66 \text{ dB}, +1.26^{\circ}$	

D. Effect of Pattern Variation on Performance of Interference Canceling

Now we consider the performance of the model function $\Phi(\theta(t))$ in the application depicted in Fig. 2; that is, as a means to mitigate the time variation induced by pattern and

thereby avoid bias in the estimation of waveform parameters in CTC. In this case the variation in $|\tilde{\Phi}(t)|$ is reduced to the variation of the ratio:

$$\zeta(t) = \left| \frac{\tilde{\Phi}(t)}{\Phi(t)} \right| \tag{16}$$

The upper bound on residual interference, I_{UB} , becomes (see [3] Equation 3.10):

$$I_{UB} \stackrel{\text{def}}{=} \left[1 - \frac{\left| \frac{\tilde{\Phi}(t+\tau)}{\Phi(t+\tau)} \right|}{\left| \frac{\tilde{\Phi}(t)}{\Phi(t)} \right|} \right]^{2} = \left[1 - \underbrace{\frac{\zeta(t+\tau)}{\zeta(t)}}_{|\Psi(t,\tau)|} \right]^{2}$$

$$I_{UB} = \left[1 - |\Psi(t,\tau)| \right]^{2}$$
(18)

The performance of the models can be quantified by comparing τ_a , the time required for pattern value update, defined in [2] and [3] as the value of τ required to achieve a specified I_{UB} for a satellite at the -3 dB point in the main lobe¹. For an ideal model (i.e., $\tilde{\Phi} = \Phi$), τ_a is unbounded, and τ_a becomes shorter as the model becomes worse. Now we estimate τ_a for the examples considered in Sections III-A-III-C; i.e., transit of a LEO satellite interferer with $\omega_a = 0.550^{\circ}$ /s (worst case scenario for Iridium as discussed in [3]). For easier comparison of the results, we normalize $\zeta(t)$ by $\zeta(t_{HP})$, where t_{HP} is the time corresponding to the -3 dB point in the main lobe. Note that this normalization does not change Ψ , so I_{UB} is not affected by this normalization.

Figs. 11–15 show normalized $\zeta(t)$ for the various examples considered in Sections III-A-III-C. Normalized $\zeta(t)=1\pm0.0316$ corresponds to $I_{UB}=0.001~(-30~{\rm dB})$. Note that the values of τ_a are significantly different on the two sides of the $-3~{\rm dB}$ point. These values correspond to the satellite moving toward or away from the reflector pointing direction. Both values of τ_a are considered since the "estimate interference waveform" block in Fig. 2 must accommodate the possibility of the satellite moving in either direction.

Fig. 11 shows normalized $\zeta(t)$ for the uncorrected true pattern $\tilde{\Phi}(t)$. This corresponds to the scenario addressed in [2] and [3]. The values of τ_a can be predicted using (see [3] Equation 3.34)

$$\tau_a \approx \frac{0.654 \,\lambda \,\sqrt{I_{UB}}}{\omega_a D} \tag{19}$$

The values of τ_a obtained from Fig. 11 are 25.5 ms and 26.0 ms. These values are comparable to the prediction of $\tau_a=23.9$ ms by (19) (using $\lambda=0.2$ m, $I_{UB}=0.001, \omega_a=0.550^\circ$ /s, and D=18 m). Even with the assumptions considered in the derivation of (19), the predicted value of $\tau_a=23.9$ ms is very close to the values estimated from the actual pattern variation.

Fig. 12 shows normalized $\zeta(t)$ for model pattern $\sqrt{G}F(t)$ described in previous section. The values of τ_a obtained from Fig. 12 are 355.1 ms and 1627.8 ms. Comparison with

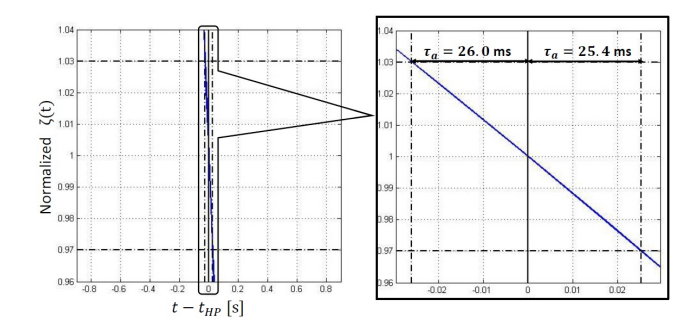


Fig. 11. Normalized ζ for the uncorrected true pattern $\tilde{\Phi}(t)$. This corresponds to the scenario addressed in reference [2].

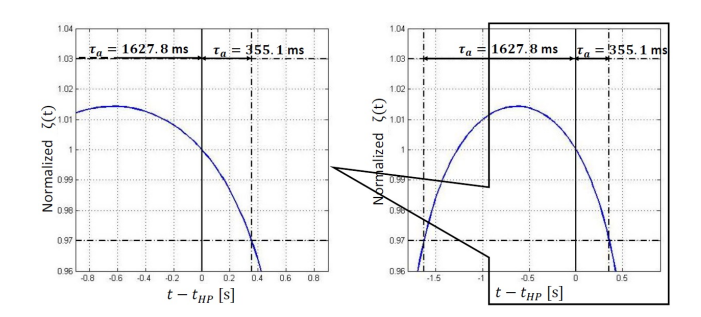


Fig. 12. Normalized ζ for model pattern $\sqrt{G}F(t)$.

Fig. 11 shows that τ_a increases by orders of magnitude using this non-adaptive model pattern.

Fig. 13 shows normalized $\zeta(t)$ for p=1 correction with constraint angle $\theta_1 = 0^{\circ}, +0.35^{\circ}, \text{ and } +1.10^{\circ}$ corresponding to Figs. 4(b), 6, and 5(b). It is surprising that the values of τ_a obtained with different constraint angles are equal. Further, these values are equal to that obtained from the uncorrected model pattern $\sqrt{G}F(t)$. A possible reason is that the shape of the pattern in all these scenarios is identical, although the absolute value for the pattern is different. Fig. 14 shows normalized $\zeta(t)$ for p=2 correction with constraint angles $\theta_1 = 0^{\circ}$, $\theta_2 = +0.35^{\circ}$ and $\theta_1 = 0^{\circ}$, $\theta_2 = +1.10^{\circ}$, corresponding to Figs. 8 and 9. The values of τ_a increase for p = 2 as compared to p = 1, indicating improvement. However, contrary to p = 1, the values of τ_a are very different for different constraint angles selected on the pattern. The values of τ_a are larger when both the constraint angles are in the main lobe as compared to the scenario when one constraint point is in sidelobe and one in main lobe. Table III summarizes values of τ_a obtained from Figs. 11-14.

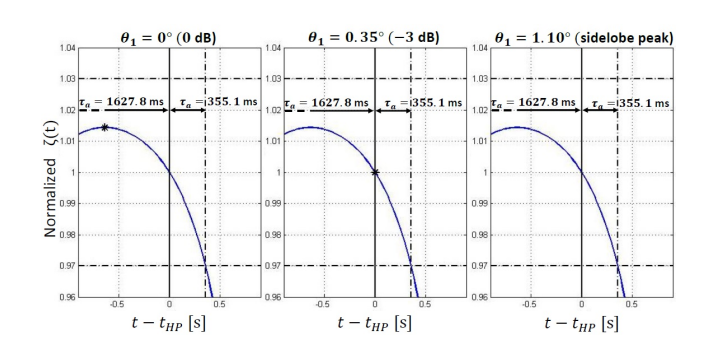


Fig. 13. Normalized ζ for model pattern $\Phi(t)$ for p=1 corresponding to Figs. 4(b), 6 and 5(b).

 $^{^1} au_a$ is the maximum duration for which residual interference is less than a specified upper bound (I_{UB}) , assuming (1) the entire duration is used for waveform estimation, (2) the only impairment to canceling is pattern variation, and (3) the interferer is located at the -3 dB point on the main lobe.

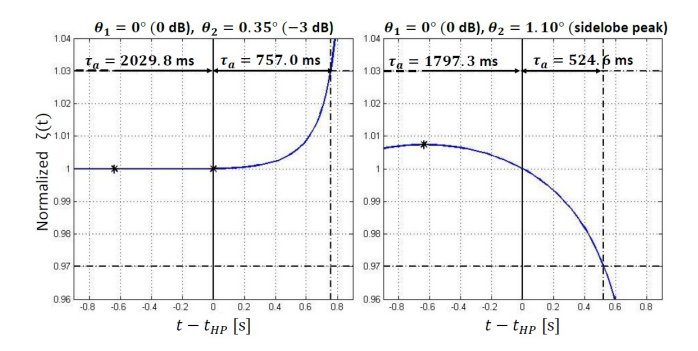


Fig. 14. Normalized ζ for model pattern $\Phi(t)$ for p=2 corresponding to Figs. 8 and 9.

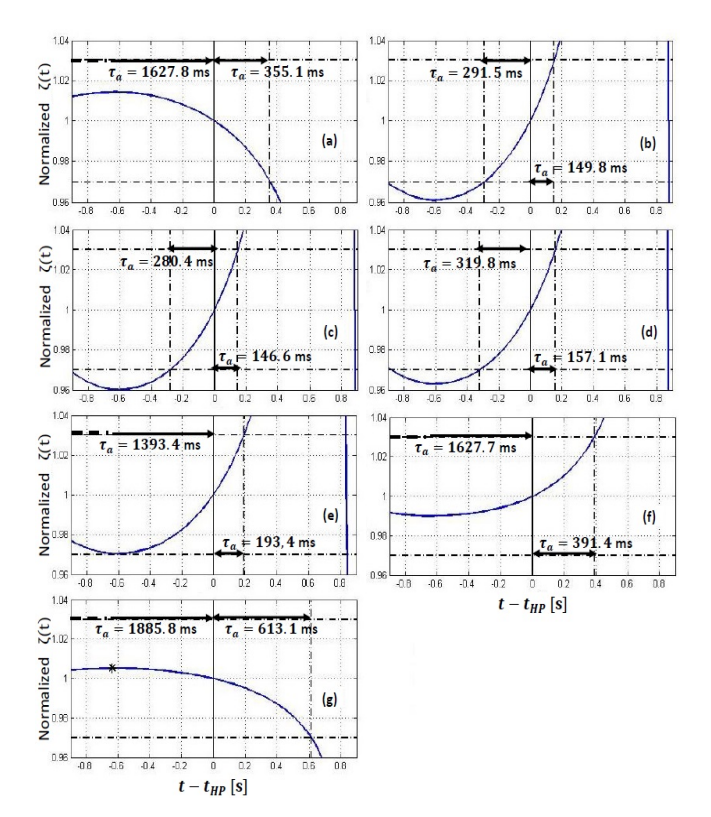


Fig. 15. Normalized ζ for model pattern $\Phi(t)$ for adaptive correction corresponding to Fig. 10. Frames (a)-(g) correspond to the frames (a)-(g) of Fig. 10.

Fig. 15 shows normalized $\zeta(t)$ for adaptive modeling corresponding to Fig. 10. The τ_a values are indicated on the frames. As observed in Fig. 10 and already discussed in Section III-C, one-point correction yields a better pattern model when constraint points are in the sidelobes, hence frame (a) shows larger values of τ_a as compared to frames (b) to (e). Frame (f) (corresponding to one constraint point in first sidelobe) has similar τ_a values as frame (a). Frame (g) with one constraint point in the main lobe has larger τ_a as compared to frame (a). Tables III and IV confirm that increasing the number of points in the adaptive modeling increases the quality of the pattern model. As was noted in Section III-C, we observe that p = 1 gives a better model when there are no constraint points in the main lobe and the first sidelobe. In general, it is confirmed that the pattern modeling increases the value of τ_a , and the adaptive modeling increases it further.

TABLE III Summary of au_a achieved for various models (Figs. 11-14).

Scenario	τ_a on the left of $-3dB$	τ_a on the right of $-3dB$	
	point in the main lobe	point in the main lobe	
True pattern $\tilde{\Phi}(t)$ (i.e., no correction)	26.0 ms	25.5 ms	
$\sqrt{G}F(t)$ (i.e., not adaptive)	1627.8 ms	355.1 ms	
$\Phi(t)$ for $p = 1$			
$(\theta_1 = 0.00^{\circ}, +0.35^{\circ}, +1.10^{\circ})$	1627.8 ms	355.1 ms	
$\Phi(t)$ for $p = 2$			
$(\theta_1 = 0.00^\circ, \theta_2 = +0.35^\circ)$	2029.8 ms	757.0 ms	
$\Phi(t)$ for $p = 2$			
$\theta_1 = 0.00^{\circ}, \theta_2 = +1.10^{\circ})$	1797.3 ms	524.6 ms	

TABLE IV Summary of τ_a achieved for various models (Fig. 15(a)-(g) corresponding to Fig. 10(a)-(g)).

Scenario	τ_a on the left of $-3dB$	τ_a on the right of $-3dB$
	point in the main lobe	point in the main lobe
p = 1 (Fig. 10(a))	1627.8 ms	355.1 ms
p = 2 (Fig. 10(b))	291.5 ms	149.8 ms
p = 3 (Fig. 10(c))	280.4 ms	146.6 ms
p = 4 (Fig. 10(d))	319.8 ms	157.1 ms
p = 5 (Fig. 10(e))	1393.4 ms	193.4 ms
p = 6 (Fig. 10(f))	1627.7 ms	391.4 ms
p = 7 (Fig. 10(g))	1885.8 ms	613.1 ms

IV. CONCLUSIONS

In this paper, we have described adaptive correction methods for the pattern function of a large axisymmetric reflector antenna. The efficacy of the methods is demonstrated by comparing the model pattern $\Phi(\theta)$ with true pattern $\tilde{\Phi}(\theta)$ obtained from PO and uncorrected pattern $\sqrt{G}F(\theta)$. It is confirmed that the adaptively corrected model patterns yield a closer fit to the true pattern as compared to $\sqrt{G}F(\theta)$, but the amount of improvement is not consistent and is small relative to the fit obtained from $\sqrt{G}F(\theta)$.

We considered correction methods in increasing order of complexity; i.e., from one-point (p=1) correction method to multi-point $(p\geq 2)$ correction method. Both the one-point and two-point correction methods were found to reduce the error in pattern modeling substantially as compared to uncorrected pattern. From the examples given in the Section III-C, we infer that the one-point correction method yields a better pattern model when constraint points are in the sidelobes and multi-point correction $(p\geq 2)$ yields better pattern model when at least one of the constraint points lies in the main lobe. The rate of pattern value update τ_a for the uncorrected pattern was found to be few milliseconds to few tens of milliseconds [2], [3]. It has been demonstrated that using the scheme shown in Fig. 2 with the pattern models proposed here, τ_a can be extended by orders of magnitude.

REFERENCES

- S.W. Ellingson, and R.M. Buehrer, "Coherent Time-Domain Canceling of Interference for Radio Astronomy," *Astron. Soc. Pac.*, Vol. 134, Art. 1041505(21pp.), Nov. 2022. DOI: 10.1088/1538-3873/ac9b92.
- [2] R. Sengupta and S.W. Ellingson, "Effect of Antenna Pattern on Time-Domain Canceling of Interference from Satellites," *IEEE International Symposium on Antennas and Propagation*, Portland, Oregon, USA, July 23–28, 2023.
- [3] R. Sengupta, "Adaptive Pattern Modeling for Large Reflector Antennas," M.S. thesis, Bradley Department of Electrical and Computer Engineering, Virginia Tech, Blacksburg, Virginia, 2022.
- [4] W.L. Stutzman and G.A. Thiele, Antenna Theory and Design, 3rd ed., Wiley, 2013.